Article

Temperature Effects and Activation Barriers in Aqueous Proton-Uptake Reactions

Balázs Antalicz* and Huib J. Bakker*

Cite This: *JACS Au* 2024, 4, 2995−3006

Read Online

ACCESS | Metrics & More | Article Recommendations | Supporting Information

ABSTRACT: Aqueous proton transfer reactions are fundamental in biology and chemistry, yet kinetics and mechanisms of strong base—weak acid reactions are not well understood. In this work, we present a temperature-dependent reaction kinetic study of the water-soluble photobase actinoquinol, in the presence and absence of succinimide, a weak acid reaction partner. We study the temperature dependence of the reaction and connect the observed dynamics to the reaction's thermodynamics. We find that actinoquinol reacts in associated complexes with water/succinimide, creating an intermediate complex that can undergo either dissociation to create products, or reverse proton transfer within the complex to recreate the initial reactants. We find that the intermediates' formation is energetically unfavorable with both reaction partners, which impacts the net reaction rates. We also find that the net reaction rate is additionally strongly influenced by the competition between the dissociation of the intermediates and their reverse reaction.

KEYWORDS: *aqueous systems, photobase, proton-uptake, proton transfer, reaction mechanism, femtosecond infrared spectroscopy, transient-absorption spectroscopy, UV−vis spectroscopy*
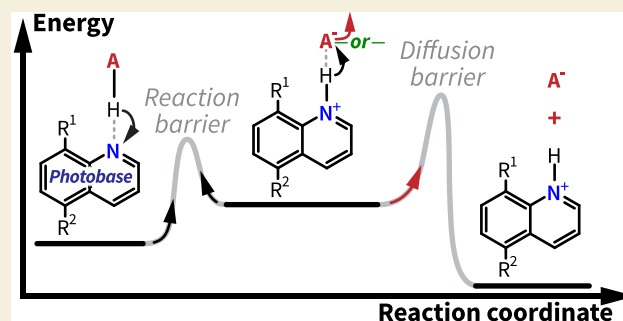
1. INTRODUCTION

Aqueous proton transfer is essential in various biological processes, such as enzymatic reactions,[1] the regulation of photosynthesis,[2] or the infection mechanism of flu.[3,4] By studying the molecular-scale mechanisms, it becomes possible to create new applications, which involve fuel cells[5] and energy storage;[6−10] or optical control over proton conductivity,[11] pH,[12−14] and chemical reactions.[15,16]

Past studies have primarily focused on photoactivated acids, and studied their proton release dynamics to the solvent,[14,17−24] and to an added reaction partner.[25−32] These studies showed that proton transfer from a photoacid to the solvent takes place on the picosecond to nanosecond timescale, while proton transfer directly to a weak base can occur on the femtosecond timescale. It was found that in water such direct reactions can also happen in reactant complexes separated by the solvent. In such complexes, protons hop from acid to base in a concerted manner, over a short-lived hydrogen-bonded chain of water molecules, i.e. a transient 'water-wire'.

Photoactivated bases have been much less studied, and prior studies have almost exclusively focused on the dynamics of the reaction with the solvent; for both Arrhenius-type[33] (ROH* → R⁺* + OH⁻) and Brønsted-type[34−40] (B* + ROH → BH⁺* + RO⁻) photobases. Similarly to photoacids, the time scale of these reactions also takes place on a picosecond to nanosecond timescale.

Recently, we reported on the reaction dynamics[41] of actinoquinol, a water-soluble, reversible, Brønsted-type photobase; in absence and in the presence of succinimide, a weak acid reaction partner. We then compared our results to a previously studied photoacid (HPTS) − weak base (acetate) reaction system,[25−29] in which the reaction partners had very similar thermodynamic driving forces compared to the photobase—weak acid system. Despite this, we found that the kinetics and the mechanisms of the two reaction systems do not match: in the photobase—weak acid system, reaction rates are significantly lower; and reactions only took place in contact pairs of reaction partners. We assessed that such differences in reaction mechanisms might be connected to more fundamental differences in transport mechanisms[42−44] of aqueous H⁺ and OH⁻.

Despite recent developments, information about the reaction mechanisms of photobases is still scarce. In this work, we perform temperature-dependent fluorescence and ultrafast mid-infrared transient absorption measurements to decipher the reaction mechanism of actinoquinol with water and with the weak acid succinimide. We find that these reactions rely on a
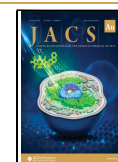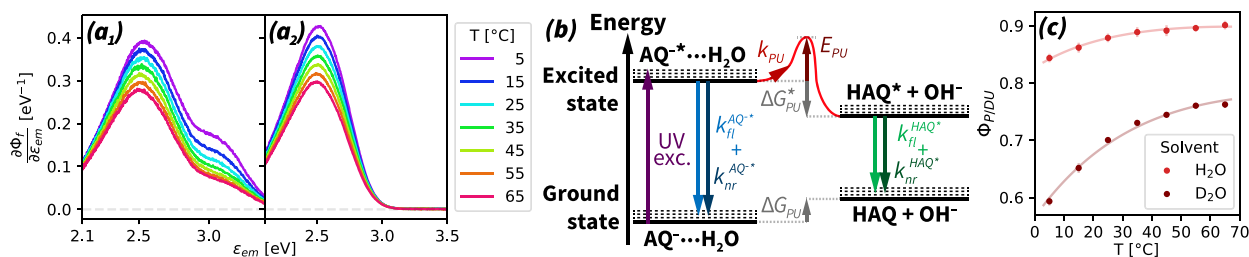
Figure 1. ($a_{1,2}$) Absolute fluorescence quantum yield (Φ_f) spectra of (a_1) actinoquinol (AQ^-) at neutral pH, and (a_2) its protonated form (HAQ) at low pH (pH $\ll$ pK_a^{HAQ} = 4.15); plotted as a function of the emitted photon energy (ε_{em}). Displayed spectra are recorded at different temperatures (T) at ε_{exc} = 3.65 eV excitation energy (λ_{exc} = 340 nm excitation wavelength). The ε_{em} = 2.5 eV band originates from HAQ*, while the ε_{em} = 3 eV band originates from AQ^{-}*. (b) Jablonski diagram of AQ^-, including the proton uptake reaction. k_{PU}: proton uptake rate; E_{PU}: activation barrier of k_{PU}; ΔG_{PU}^* and ΔG_{PU}: free energy changes driving the excited/ground-state reactions; k_{fl} and k_{nr}: rates of excited-state decay via fluorescent and nonradiative means. (c) Temperature effect on the quantum yield of the proton uptake reaction in water (Φ_{PU}) and heavy water (Φ_{DU}). Solid lines are based on trend fits in Figures S12 and S13.

two-step mechanism, which involves an intermediate hydrogen-bonded complex that can either dissociate into reaction products or undergo a reverse proton transfer reaction to restore the initial reactant complex. We find that the competition of these processes strongly influences both the rate and the effective energy barrier of the overall reaction. Based on the new experimental insights, we develop a theoretical framework that accounts for both the kinetics and the thermodynamic properties of the reaction system, provides a detailed understanding of the mechanism of proton uptake reactions, and explains the nontrivial dependence of the rate of these reactions on temperature and on reactant concentrations.

2. RESULTS AND DISCUSSION

2.1. Temperature-Dependent Photobasic Properties of Actinoquinol

In Figure 1a$_{1-2}$, we study the temperature-dependent fluorescence emission spectra of actinoquinol at neutral pH (AQ^-, Figure S1a), and its protonated form at lower pH (HAQ, Figure S1b). In Figure S5, we show similar spectra recorded in heavy water (D_2O). In both solvents, we find that exciting AQ^- at neutral pH/pD yields two fluorescent emission bands: one at 3 eV (410 nm) and one at 2.5 eV (500 nm). Because the 2.5 eV emission band is identical to the one observed after exciting H/DAQ at lower pHs/pDs, we assign the band to emission from excited-state H/DAQ*. Similarly, we assign the 3 eV emission band to originate from AQ^{-}*. Because exciting AQ^- yields H/DAQ* bands in both solvents, we conclude that it is the result of the AQ^{-}* ···H/D$_2$O → H/DAQ*+OH$^-$/D$^-$ proton uptake reaction. This then shows that AQ^- is photobasic, which is a common property of quinoline derivatives.[45,46] To summarize these conclusions, we present a Jablonski diagram in Figure 1b. Here, we depict the term levels of AQ^- and HAQ, as well as the ΔG_{PU}^* and ΔG_{PU} free energy changes that drive the excited- and ground-state proton uptake reactions. Using these terms, we could previously[41] establish that photoexcitation changes the basicity of actinoquinol from pK_b = 9.85 to pK_b^* = 0.75, explaining its enhanced reactivity in the excited-state.

In Figure 1b, we also show the competition of the proton uptake reaction, described with the first-order rate of k_{PU}; and the fluorescent and nonradiative decay channels, described with the rate constants $k_{fl}^{AQ^{-}*}$ and $k_{nr}^{AQ^{-}*}$, respectively. Using this notation, we derive that the quantum yield of the proton uptake reaction is

$$\Phi_{PU} = k_{PU}/(k_{PU} + k_{fl}^{AQ^{-}*} + k_{nr}^{AQ^{-}*}) \tag{1}$$

To study the temperature-dependence of Φ_{PU}, we use log-normal band fitting[47,48] to determine the areas of the emission bands of AQ^{-}* and HAQ*. To do this, we use the assumptions that emission bands are identical in both H_2O and D_2O, and that all band parameters (i.e., center, width, asymmetry) vary linearly with temperature. We show fit results in Figures S6 and S7, and summarize the fitting parameters in Figures S8–S10. The obtained emission band areas then describe the conditional probabilities (P_f) of observing fluorescent emission (↓) by exciting (↑) either of the photobase forms. Using this notation, we derive the following:

$$\Phi_{PU} = P_f^{AQ^-\uparrow, HAQ^*\downarrow}(\text{neutral pH})/\Phi_f^{HAQ^*}(\text{low pH}) \tag{2}$$

We then show its temperature dependence in Figure 1c. We find that Φ_{PU} is greatly enhanced with increasing temperature: in the 5−65 °C range, Φ_{DU} increases from 59 ± 1% to 76 ± 1%, while Φ_{PU} increases from 84 ± 1% to 90 ± 1%. Such an increase in Φ_{PU} suggests that the activation barrier of the proton uptake reactions (E_{PU}, see Figure 1b) is much larger than the effective activation barrier of the competing fluorescent and nonradiative relaxation channels.

Next, we use the P_f values to obtain information about the dynamics of the proton uptake process. Using the notation in Figure 1b, we derive that

$$P_f^{AQ^-\uparrow, AQ^{-}*\downarrow} = k_{fl}^{AQ^{-}*}/(k_{PU} + k_{fl}^{AQ^{-}*} + k_{nr}^{AQ^{-}*}) \tag{3}$$

In turn, this yields that $\Phi_{PU}/P_f^{AQ^-\uparrow, AQ^{-}*\downarrow} = k_{PU}/k_{fl}^{AQ^{-}*}$. We show the obtained $k_{PU}/k_{fl}^{AQ^{-}*}$ trends in Figure S12. Assuming that $k_{fl}^{AQ^{-}*}$ is identical for AQ^{-}* in both H_2O and D_2O, we calculate the k_{PU}/k_{DU} ratios at different temperatures. We find that this kinetic isotope effect changes from 3.6 ± 0.07 at T = 5 °C to 3.0 ± 0.04 at T = 65 °C; see Figure 2a. By plotting the k_{PU}/k_{DU} ratios in an Arrhenius plot, we determine its slope: $-\partial \ln(k_{PU}/k_{DU})/\partial \beta$ = $E_{PU} - E_{DU}$ = −2.4 kJ/mol, where we defined $\beta = (R \cdot T)^{-1}$.

2.2. Temperature Effect in Aqueous Proton Uptake Reactions

To study the dynamics of aqueous proton uptake reactions of AQ^-, we performed UV-pump−IR-probe experiments with ε_{exc} = 3.63 eV (λ_{exc} = 342 nm) pump pulses and tunable IR probe pulses in the $\tilde{\nu}$ = 1420−1580 cm^{-1} region, up to a maximal pump−probe delay of τ_{pp} = 2.3 ns.
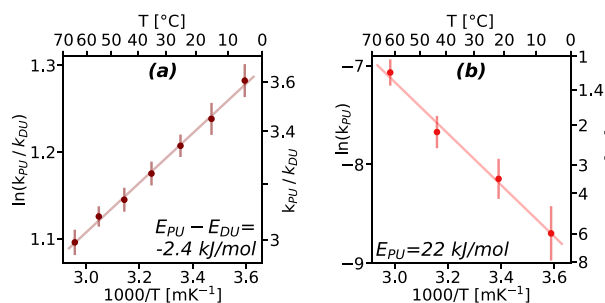
Figure 2. Arrhenius plots for (a) k_{PU}/k_{DU}, from fluorescence measurements in Figure 1, used to obtain $E_{PU}-E_{DU}$; and for (b) k_{PU}, from transient absorption measurements in Figure 4, used to obtain E_{PU}. Error bars in are in 95% confidence intervals in (a), and manual estimates in (b). In both figures, solid lines are linear trend fits.

In Figure 3a, we show the infrared absorption spectrum of AQ$^-$ at $T = 22$ °C, which has a prominent feature at $\tilde{\nu}$ = 1507 cm^{-1} and a number of smaller absorption peaks at lower frequencies. The main $\tilde{\nu}$ = 1507 cm^{-1} band also has a slightly different frequency and width in D$_2$O (Figure S22), suggesting that this band is sensitive to the hydrogen-bonding environment. In Figure S21a, we decompose the full absorption spectrum as a set of Lorentzian peaks; see Table S2.

In Figure 3b, we analyze the transient absorption spectra of photoexcited AQ$^-$*. Here, we observe a number of weaker positive features alongside the strong ground-state bleach of AQ$^-$ at 1507 cm^{-1}. At early pump–probe delays ($\tau_{pp} < 30$ ps), these features show mild frequency shifts due to solvent relaxation, see Figure S24. We model the relaxation of these signals with the rate constant k_{solv}.

At longer pump–probe delays, we find that the observed transient absorption signals change over several nanoseconds. More specifically, we observe the rise and saturation of HAQ* peaks at the spatial frequencies of $\tilde{\nu}$ = 1427 and 1465 cm^{-1}. These features match those observed by directly exciting HAQ; see Figure S23. In Figure 4a$_1$–d$_1$, we show the dynamics at 1469 cm^{-1} at different temperatures; see the c^{HSI}=0 M curves. At this frequency, the transient absorption of AQ$^-$* is very small; thus, the observed dynamics primarily originate from HAQ*. At higher temperatures, HAQ* generation gets increasingly faster, suggesting a large activation barrier. This is in accordance with the fluorescence measurements, which showed that k_{PU} increases much faster with temperature than $k_{fl}^{AQ^-}$ (Figure S12).

Next, we study the dynamics in the 1550–1565 cm^{-1} region, see Figures 3b and S26. These dynamics are complex and show a c^{AQ^-}-dependence. Notably, HAQ also absorbs in this spectral region, at $\tilde{\nu}$ = 1558 cm^{-1} (Figures 3a and S26e). Because the AQ$^-$* dynamics at 1507 cm^{-1} are not affected (Figure S26c), we infer that the c^{AQ^-}- dependence of the observed dynamics is a result of HAQ* being quenched by AQ$^-$. Similar quenching behavior has been previously observed in case of the photoacid HPTS, which also affected its observed proton release dynamics.[29] We model this quenching effect with an additional term for the excited-state decay rate constant of HAQ*:

$$k_{ES}^{HAQ*}(c^{AQ^-}) \approx k_{ES}^{HAQ*}(c^{AQ^-}=0) + c^{AQ^-} \cdot k_{quench} \quad (4)$$

Here, we approximate that $k_{ES}^{HAQ*}(c^{AQ^-}=0) \approx k_{ES}^{AQ^-*} \approx k_{fl}^{AQ^-*}$.

To reason the latter approximation, we consider that the efficiency of nonresonant relaxation method of AQ$^-$* is quite
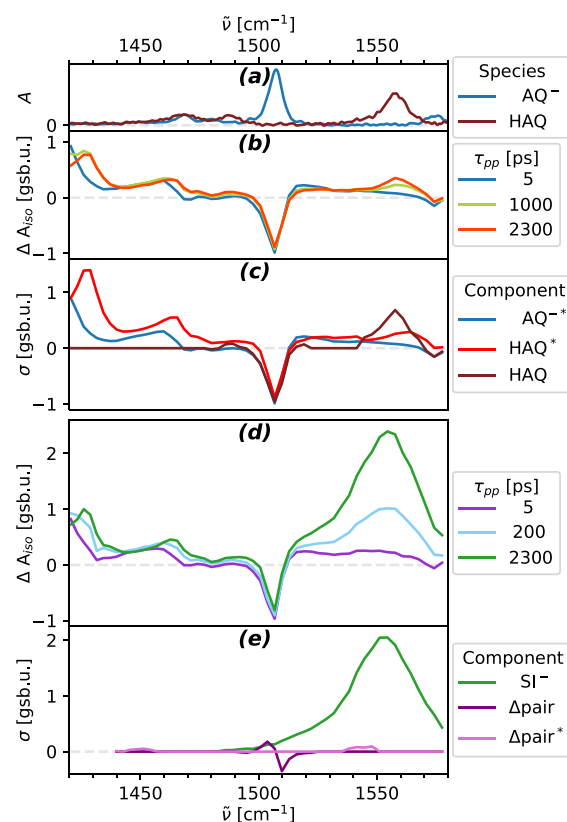
Figure 3. (a) Steady-state absorption spectra (A) of AQ$^-$ and HAQ in H$_2$O at $T = 22$ °C, plotted in function of the spatial frequency ($\tilde{\nu}$) of the absorbed infrared light. Spectra are displayed after solvent feature subtraction and are normalized with sample concentration and thickness; see Supporting Information. (b) Transient absorption spectra (ΔA_{iso}) of 20 mM AQ$^-$ in H$_2$O at $T = 62$ °C, obtained at different probe pulse delays (τ_{pp}) after a $\varepsilon_{exc} = 3.63$ eV ($\lambda_{exc} = 342$ nm) pump pulse. On the vertical axis, 1 gsb. u. (≈ 0.6 mOD at $c^{AQ^-} = 10$ mM) is defined as the magnitude of the 1507 cm^{-1} ground-state bleach of AQ$^-$ at short pump–probe delays. (c) Component-associated spectra (σ) of different photobase species, extracted from measurements in neat H$_2$O. (d) Transient absorption spectra of 10 mM AQ$^-$ with 2 M succinimide (HSI) added, in H$_2$O at $T = 62$ °C. (e) Component-associated spectra extracted from HSI-containing solutions. SI$^-$ denotes deprotonated succinimide, while 'Δpair$^{(*)}$' refers to the absorption difference between HSI-associated and free AQ$^{-(*)}$. For solutions with added HSI, we omit the $\tilde{\nu} < 1439$ cm^{-1} region from our analysis; because the additional absorption of HSI increases noise and overlaps with complex contributions from SI$^-$, Δpair$^{(*)}$ and HAQ*.

low at all temperatures (Figure S11). We also assess that $k_{nr}^{AQ^-*}$ is slightly different in H$_2$O and D$_2$O, see Figure S13. Such differences can arise in case of intersystem crossing (ISC), which is quite common in quinolines.[34] Here, differences in vibrations (Figure S22) can lead to differences in vibrational couplings[49] that influence the net rate of the process. This is something also found in case of HAQ* and DAQ* where $k_{nr}^{H/DAQ*}$ showed a strong isotope dependence[41] (Figure S13). Because ISC leads to triplet states that are typically long-lived, we assess that $k_{nr}^{AQ^-*}$ does not have meaningful contributions to the replenishment of ground-state AQ$^-$ and thus approximate $k_{ES}^{AQ^-*} \approx k_{fl}^{AQ^-}$. In the case of HAQ*, we first study its transient absorption features in Figure S23. In the measurement window, we find only a weak decay, and no vibrational changes associated with intersystem
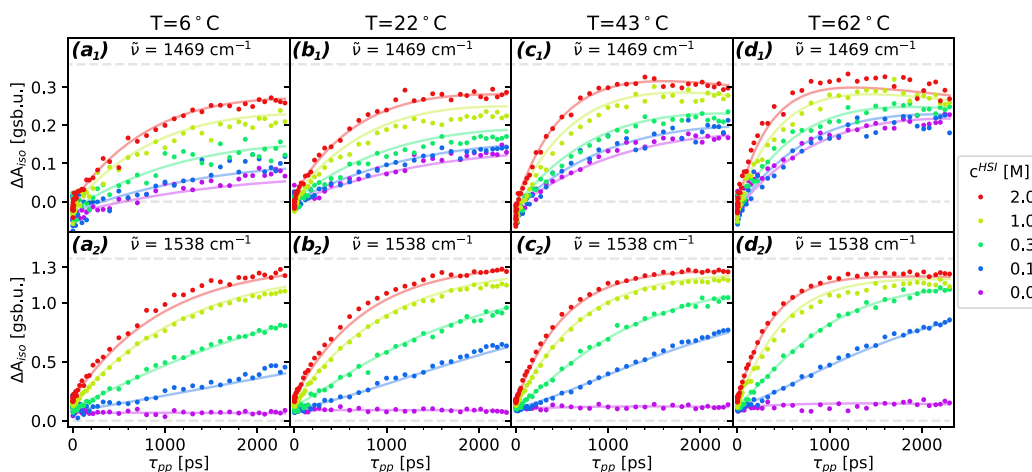
Figure 4. Normalized transient absorption signals of obtained by exciting AQ^-, in a solution with different concentrations of added succinimide (c^{HSI}), recorded at different pump–probe delays and temperatures: T = (a) 6 °C, (b) 22 °C, (c) 43 °C, (d) 62 °C. At the top (a_1–d_1), we show absorption dynamics recorded at $\tilde{\nu}$ = 1469 cm^{-1}, which primarily originate from HAQ*. At the bottom (a_2–d_2), we show dynamics at $\tilde{\nu}$ = 1538 cm^{-1}, which primarily originate from SI$^-$. Dots represent raw data points, and solid lines represent best fits based on the reaction model presented in the main text. Signals are normalized based on the $\tilde{\nu}$ = 1507 cm^{-1} ground-state bleach feature of AQ^-; see protocol description in the Supporting Information.

crossing. We thus consider that the decay is likely due to self-quenching and approximate that $k_{ES}^{HAQ*}(c^{AQ^-} = 0) \approx k_{ES}^{AQ^-*}$. We assess the error of this approximation to be quite low, considering that the thus obtained time-constants (Figures S12 and 2b) are at least ten times the length of the observed 2.3 ns delay window.

We then perform broadband kinetic modeling on the presented data set and show the photobase-related species-associated spectra (σ) in Figure 3c. The obtained σ^{HAQ*} offers a good match to the features obtained by exciting HAQ (Figure S23), and σ^{HAQ} features too match the absorption difference of HAQ and AQ^- (Figures 3a and S21). This suggests that our model offers an accurate description of the quenching process. We additionally find that the recovered k_{quench} values (Figure S27) do not follow the $k_{quench}(T) \propto D(T) \propto T$ trend predicted from the Einstein–Smoluchowski relation,[50] but instead decrease with increasing temperature. This suggests that the method of quenching is not primarily driven by random collisions.

Next, we study the obtained k_{PU} values in Figure 2b. We find that these form a straight line on the Arrhenius plot with the following slope: E_{PU} = 22 kJ/mol. This value is quite high: it is even larger than the $E_{H-bond reorg.}$ = 16.5 ± 2.5 kJ/mol literature value[51−58] of the activation energy for the reorganization of the hydrogen-bond network in neat water.

### 2.3. Temperature Effect in Bimolecular Proton Uptake Reactions

We additionally study the bimolecular reaction between AQ^-* and succinimide (HSI, Figure S1c), a weak acid reaction partner (pK_a = 9.56).[59] In Figure 3d, we show transient absorption spectra obtained by exciting AQ^-, at T = 62 °C in H_2O, with c^{HSI} = 2 M. When compared to transient absorption experiments in neat H_2O, the signals at $\tilde{\nu}$ = 1427 and 1465 cm^{-1} are enhanced at all delays. We additionally observe a broadband absorption signal around $\tilde{\nu}$ = 1557 cm^{-1}, corresponding to absorption of deprotonated succinimide (SI$^-$, Figure S1d). The shape, width and frequency of this signal matches the previously identified signals,[41] and has been assigned to the asymmetric C=O stretching vibration of the SI$^-$ ion.[60]

In Figure 4a_2–d_2, we display transient absorption signals at $\tilde{\nu}$ = 1538 cm^{-1}, showing the dynamics of SI$^-$ generation. This choice of frequency allows us to distinguish SI$^-$ signals from the overlapping, but narrower HAQ$^{(*)}$ signals near $\tilde{\nu}$ = 1558 cm^{-1}. With an increase in temperature, the deprotonation reaction of HSI becomes much faster, regardless of c^{HSI}. At T = 62 °C and at c^{HSI} = 2 M, the SI$^-$ signal reaches its maximal value already at τ_{pp} = 1000 ps, whereas it does not fully saturate by τ_{pp} = 2300 ps at T = 6 °C. Furthermore, notable differences appear in the end-level signals at τ_{pp} = 2300 ps for c^{HSI} = 0.1 M: at T = 62 °C, the end-level is approximately twice as big as the end-level at T = 6 °C.

To model the reaction kinetics of AQ^-* and HSI in H_2O, we consider two parallel reaction pathways. In the first reaction pathway, we describe the (1A) $AQ^-* \cdots H_2O \rightarrow HAQ* + OH^-$ proton-uptake with rate constant k_{PU}, and the subsequent (1B) $OH^- + HSI \rightarrow H_2O + SI^-$ neutralization with the rate constant $k_{neut} \cdot c^{HSI}$. This pathway dominates at low c^{HSI}, where a small c^{HSI} increase yields a large SI$^-$ enhancement but a small relative HAQ* enhancement. In the second reaction pathway, we consider the formation of directly associated actinoquinol-succinimide reactant pairs and their direct proton transfer reaction: (2A) the $AQ^-* \cdots HSI \rightarrow HAQ* \cdots SI^-$ forward reaction with k_{HSI}^f, and (2B) the $HAQ* \cdots SI^- \rightarrow AQ^-* \cdots HSI$ reverse reaction with k_{HSI}^r. This pathway is most important at high c^{HSI}, where it leads to a significant enhancement of both the HAQ* and SI$^-$ signals.

To quantify the ratio of associated reactant pairs at τ_{pp} = 0, we need to measure their K_{assoc}^{pair} association constant. We previously reported[41] that the red-shift of the UV–vis spectrum of associated pairs can be used to extract this quantity. We describe our updated protocol in Supporting Information (Figures S14−S20), and we show our results in Figure 5a. The obtained results form a single line on the Arrhenius plot, the slope of which describes the standard enthalpy of formation: ΔH_{assoc}^{pair} = −10 kJ/mol. The large negative value shows that the pair formation of the reactants is energetically favorable.

In the reaction model, we additionally include the ongoing equilibration of free and associated reactants with rate constants k_{dissoc} for dissociation and $k_{assoc} \cdot c^{HSI}$ for association. To establish and maintain the hydrogen-bond in associated pairs, the
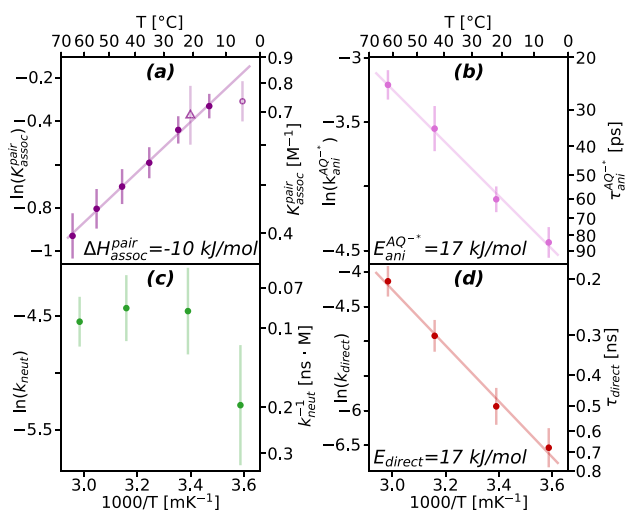
Figure 5. (a) Van't Hoff plot for K_{assoc}^{pair}, the steady-state association constant of AQ^{-*} and HSI in H_2O, used to obtain the standard reaction enthalpy ΔH_{assoc}^{pair}. (b–d) Arrhenius plots for (b) $k_{ani}^{AQ^{-*}}$, the rate of anisotropy decay of AQ^{-*} due to its reorientation, used to obtain $E_{ani}^{AQ^{-*}}$; (c) k_{neut}, the rate of bulk neutralization reaction of HSI by OH^-; (d) k_{direct}, the effective rate of one-way direct reactions in the $c^{HSI} \to \infty$ limit, calculated with the second order accurate formula S45; used to obtain E_{direct}. In (b) and (d), solid lines are linear trend fits. In (a), the solid line gives the best global fit for $\ln(K_{assoc}^{pair}(T))$ for the points with solid color. The hollow circle at 5 °C is a best fit result from a partial measurement set; and the hollow triangle at 22 °C is an independent measurement with different conditions; see the Supporting Information. Displayed errors are defined in the Supporting Information.

reactants need to possess a high degree of orientational correlation. We previously assessed that reorientation by the heavier AQ^{-*} is likely the main source of the $AQ^{-*}\cdots$HSI hydrogen-bond breaking, given its impact on the immediate solvation shell of the reactant pair. Using polarization-resolved measurements, we measure $k_{ani}^{AQ^{-*}}$, the anisotropy loss rate of AQ^{-*} due to its reorientation; see Figure 5b. We thus approximate that the dissociation rate is $k_{dissoc} \approx k_{ani}^{AQ^{-*}}$, which yields $k_{assoc} = k_{ani} \cdot K_{assoc}^{pair}$.

Similarly, we also assume that the breakup rate of $HAQ^*\cdots SI^-$ pairs is also $k'_{dissoc} = k_{dissoc} \approx k_{ani}^{AQ^{-*}}$. We additionally neglect the back-diffusion process: since SI^- is a small ion, it reorients much faster than actinoquinol ($k_{ani}^{SI^-} \gg k_{ani}^{AQ^{-*}}$), meaning that the orientation of a just-dissociated SI^- will quickly change. This then leads to the loss of the pre-existing orientational correlation between HAQ^* and SI^-, which strongly hinders the reformation of the intermediate complex. Because $c^{SI^-} < c^{HAQ^*} \ll c^{AQ^-} = 10$ mM, scavenging an SI^- from another HAQ^* is extremely unlikely.

A final addition to the model is the inclusion of the quenching of HAQ^* by AQ^-. Previously, we found that k_{quench} decreases with the temperature, which cannot be explained with simple collision-based quenching. Instead, we propose that AQ^- can quench HAQ^* when it is hydrogen-bonded to it. Self-quenching based on hydrogen-bonding has been previously observed in other aza-aromatics.[61] This means, that k_{quench} would decrease with temperature, because the association constant of $HAQ^*\cdots AQ^-$ pairs would too. This mechanism additionally explains the c^{HSI}-dependence of k_{quench}: at higher c^{HSI}, both $AQ^-\cdots$HSI and $HAQ^*\cdots$HSI pairs emerge; which would lead to the decrease in

the rate of formation of $AQ^-\cdots HAQ^*$ complexes. We account for this with the expression:

$$k_{quench}(c^{HSI}) \approx$$
$$k_{quench}(c^{HSI} = 0) \cdot (1 - r_{assoc}^{pair}(c^{HSI})) \cdot (1 - r_{assoc}^{HAQ}(c^{HSI}))$$
$$(5)$$

Here, $r_{assoc} = K_{assoc} \cdot c^{HSI} / (1 + K_{assoc} \cdot c^{HSI})$ and K_{assoc}^{HAQ} is the association constant for $HAQ\cdots HSI$ pairs (Figure S20).

We summarize our model in Eqs. S3 and S4. This reaction model provides a good fit for the observed reaction dynamics at all temperatures and succinimide concentrations; see Figure 4 for the comparison of the dynamics. In Figure S30, we show that the residuals of the fit are very small.

In Figure 3e, we show additionally recovered component-specific spectra. Here, the broad feature of σ^{SI^-} at 1557 cm^{-1} matches both the observed late-delay transient absorption signals in Figure 3d and its linear absorption spectrum.[41,60] Based on the succinimide-containing samples, we extract the vibrational response of associated $AQ^{-(*)}\cdots$HSI species, which shows only minor differences compared to the response of $AQ^{-(*)}\cdots H_2O$ species.

In Figure 5c, we show the recovered k_{neut}, which appears to be constant at $T = 22$ °C and above, and decreases below that, i.e. at $T = 6$ °C. This trend is interesting, because all other rate and association constants form a linear trend within the Arrhenius plot. To rule out individual sample concentration errors, we repeated the experiment at $c^{HSI}=0.1$ M at $T = 6$ °C and found the results to be indistinguishable.

In Figure 5d, we show the obtained k_{direct} values, which denotes the effective one-way forward rate constant of direct reactions in the $c^{HSI} \to \infty$ limit, calculated based on the best model fit to the data (Eq. S44). Here, we do not directly show $k_{HSI}^{f/r}$ values because these have a large error covariance and thus cannot be recovered with the desired accuracy. We investigate this effect in a later section, where we show that individual contributions from $k_{HSI}^{f/r}$ are rather small and that the main physical observable is instead k_{direct}.

2.4. Dynamics and Barriers in Aqueous Proton Uptake Reactions

In the previous section, we modeled the direct proton transfer reaction in $AQ^{-*}\cdots$HSI pairs with the forward k_{HSI}^f, and the reverse k_{HSI}^r rate constants. This description relied on the inclusion of an intermediate $HAQ^*\cdots SI^-$ species.

To explore the inclusion of an intermediate in the reaction with water, we consider that the $AQ^{-*}\cdots H_2O \to HAQ^* + OH^-$ proton-uptake reaction has the following, spectroscopically invisible reaction steps: (1) $AQ^{-*}\cdots H_2O \to HAQ^*\cdots OH^-$ forward reaction with the rate constant $k_{H_2O}^f$, (2) $HAQ^*\cdots OH^- \to AQ^{-*}\cdots H_2O$ reverse reaction with the rate constant $k_{H_2O}^r$, and (3) $HAQ^*\cdots OH^- \to HAQ^*+OH^-$, representing dissociation of the intermediate complex with the rate constant k_{diff}. Similarly to the case of HAQ^* and SI^-, we do not include back-diffusion, given the spatial and orientational correlation requirements for HAQ^* and OH^- to reform a complex. We describe this system of differential equations using a rate-matrix formalism; see Supporting Information Section 6.1.

To connect $k_{H_2O}^{f/r}$ with the experimentally observed k_{PU}, we investigate the $\tau_{pp} \to \infty$ asymptotic behavior of the reaction system. The general solution is a biexponential function, which is not something we observe. However, in the $k_{H_2O}^r \gg k_{H_2O}^f$ limit,

the dynamics simplify to a single exponential (Eq. S17), with an effective rate constant of

$$k_{PU} = k^f_{H_2O} \cdot (1 - \lambda_{PU}) \tag{6}$$

Here, the factor

$$\lambda_{PU} = k^r_{H_2O} / (k_{diff} + k^r_{H_2O}) \tag{7}$$

describes the factor by which the reaction is slowed down compared to $k^f_{H_2O}$: $\lambda_{PU} = 0$ indicates no slowdown, and values of λ_{PU} approaching 1 indicate an increasing slowdown. In the $k^r_{H_2O} \gg k^f_{H_2O}$ limit, the observable reaction dynamics will be dictated by the competition of intermediate complexes' dissociation and their reverse reaction. Because the observed dynamics are monoexponential, we cannot directly determine the $k^f_{H_2O}/k^r_{H_2O}$ ratio.

In Supporting Information Section 6.1, we study the effective activation barrier in the $k^r_{H_2O} \gg k^f_{H_2O}$ limit. In Eq. S22, we obtain that

$$E_{PU} = -\partial \ln(k_{PU})/\partial\beta = E^f_{H_2O} + \lambda_{PU} \cdot (E_{diff} - E^r_{H_2O}) \tag{8}$$

Here $\beta = (R \cdot T)^{-1}$. Clearly, a larger λ_{PU} slow-down effect leads to larger E_{PU}; eventually converging to $E^f_{H_2O} + E_{diff}$ if $\lambda_{PU} \to 1$. In general, $E_{diff} \neq E^r_{H_2O}$, meaning that λ_{PU} has an implicit temperature dependence that—under certain conditions—can yield a temperature-dependence in E_{PU}. Temperature-dependent activation barriers have been previously observed for the reactions of reversible photoacids with water, for example for 2-napthtol, 2-napthtol-6,8-disulfonate,[19] and HPTS.[17] Similar to our scenario, the accurate description of these processes suggested that the dissociation of the intermediates plays a critical role and can affect the activation barrier of the overall reaction. In general, our theoretical derivation yields an effective reaction barrier E_{PU} that has a form similar to those emerging in complex reactions, proposed by earlier works.[62,63] A key difference in our approach is that we study reaction dynamics, while earlier works were based on a steady-state description.

We summarize our description in Figure 6, where we illustrate the energy levels of different chemical species. Here, we
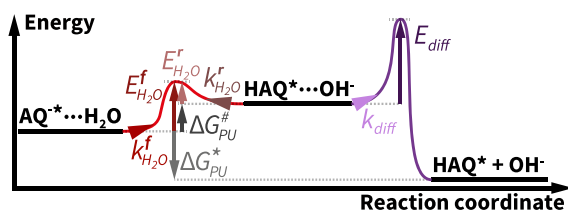
Figure 6. Eigen-Weller model for describing the excited-state proton-uptake reaction by AQ^{-*}, introducing the $HAQ^* \cdots OH^-$ intermediate state. $k^f_{H_2O}$ and $k^r_{H_2O}$ denote forward and reverse proton-uptake rate constants in the first reaction step, while k_{diff} describes the rate constant of the diffusion-driven separation of $HAQ^* \cdots OH^-$ complexes. For the sake of clarity, we omit excited-state decay channels of the photobase species but do include them in the fitting process.

introduce $\Delta G^{\#}_{PU} = E^f_{H_2O} - E^r_{H_2O}$, the energy gap between the reactants and the intermediate complex. To derive a formula connecting $k^{f/r}_{H_2O}$ and E_{PU}, we consider that if diffusion was absent, then the two complexes $AQ^{-*} \cdots H_2O$ and $HAQ^* \cdots OH^-$

would form a two-level system. In this case, their relative concentrations would follow Maxwell−Boltzmann statistics:

$$[AQ^{-*} \cdots H_2O]/[HAQ^* \cdots OH^-] = \exp(\Delta G^{\#}_{PU} \cdot \beta) \tag{9}$$

At the same time, mass conservation dictates that

$$[AQ^{-*} \cdots H_2O] \cdot k^f_{H_2O} = [HAQ^* \cdots OH^-] \cdot k^r_{H_2O} \tag{10}$$

This yields that

$$\Delta G^{\#}_{PU} \cdot \beta = \ln(k^r_{H_2O}/k^f_{H_2O}) > 0 \tag{11}$$

This expression also holds in the presence of the second (diffusion) reaction step; and suggests that even if the first reaction step to the intermediate state is not energetically favorable, the overall proton-uptake reaction can still take place ($\Delta G^*_{PU} < 0$). If the barrier of the forward reaction is large—i.e. $E^f_{H_2O} \gg E^r_{H_2O}$ — then in Eq. S30 we derive that

$$E_{PU} + \beta^{-1} \cdot \ln \frac{k_{PU}}{k_{diff}} = \beta^{-1} \cdot \ln \lambda_{PU} + E_{diff} \cdot \lambda_{PU} \tag{12}$$

To determine λ_{PU}, we need to estimate k_{diff}, the rate constant of the dissociation of the hydroxide ion from HAQ^*. We approximate that k_{diff} is identical to the rate at which OH^- ions jump over the length of a water molecule in room temperature bulk water:[64] $k_{diff} \approx (3 \ ps)^{-1}$. In this approximation, the diffusion of hydroxide is governed by the reorganization of the hydrogen-bond network of bulk water, from which it follows that[51−58] $E_{diff} \approx E_{H-bond \ reorg.} = 16.5 \pm 2.5$ kJ/mol. At 22 °C, we thus obtain that $\lambda = 0.4 \mp 0.04$, $E^f_{H_2O} \approx \Delta G^{\#}_{PU} = 15 \mp 0.3$ kJ/mol, $k^r_{H_2O} = (4.5 \pm 1 \ ps)^{-1}$ and that $k^f_{H_2O}/k^r_{H_2O} = 1/(480 \mp 50)$. If k_{diff} would be slower than this, then λ_{PU} would increase and $k^f_{H_2O}/k^r_{H_2O}$ would decrease. The above approximation for k_{diff} yields results consistent with the original $k^r_{H_2O} \gg k^f_{H_2O}$ hypothesis.

We also find that the phenomenological activation energy of the overall reaction barrier is $E_{PU} = 22$ kJ/mol, which is 7 kJ/mol larger than the $E^f_{H_2O} = 15$ kJ/mol activation energy of the forward proton-uptake reaction. Considering that $E^f_{H_2O} \approx \Delta G^{\#}_{PU}$, this means that the free energy difference between the $AQ^{-*} \cdots H_2O$ reactant complex and the $HAQ^* \cdots OH^-$ intermediate complex is quite large, 6 times the thermal energy $R \cdot T$ at room temperature. Last, we note that the obtained 40% value for the slow-down factor confirms that the competition between hydroxide diffusion and the reverse reaction indeed plays a significant role.

2.5. Dynamics and Barriers in Bimolecular Proton Uptake Reactions

Next, we unify the results of the reaction of AQ^{-*} and H_2O with the previous results for the direct reaction of AQ^{-*} and HSI; and illustrate the resulting reaction scheme in Figure 7. In Supporting Information Section 6.4, we then repeat our previous mathematical approach and obtain k'_{direct}, the one-way effective reaction rate constant of the $AQ^{-*} \cdots HSI \to HAQ^* + SI^-$ reaction. We find that k'_{direct} is dependent on both τ_{pp} and c^{HSI}. Shortly after UV excitation ($\tau_{pp} \to 0$ limit), we find that $k'_{direct} = k^f_{HSI}$ (Eq. S58). This, however, quickly decreases, as the concentration ratio of the reactant and the intermediate complexes, i.e. $[AQ^{-*} \cdots HSI]/[HAQ^* \cdots SI^-]$, quickly shifts. This process then happens with the rate of $k_{eq} \approx k^r_{HSI} + k_{dissoc}$ (Eq. S60).
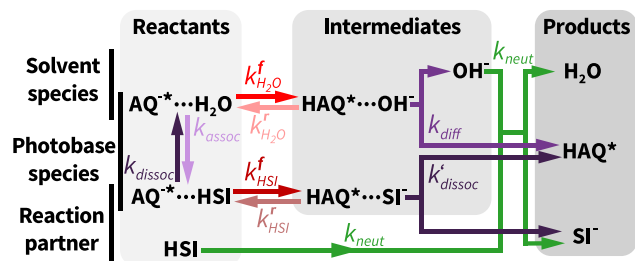
Figure 7. Reaction model for describing the bimolecular proton-uptake reaction of AQ^-* with H_2O and HSI. k_{dissoc} and k_{assoc} describe the net dissociation and association rate of the $AQ^-*\cdots$HSI reactant pairs, while k'_{dissoc} describes the net dissociation rate of $HAQ^*\cdots SI^-$ pairs. k_{neut} describes the bulk reaction rate of OH^- and HSI. For clarity of illustration, excited-state decay channels of the photobase species are omitted but are otherwise included in the fitting process.

The kinetics described above lead to fast, small-amplitude dynamics at early delays ($\tau_{pp} < 20$ ps), which evolve into much slower dynamics. In our previous work,[41] we assigned the fast, early delay dynamics to quickly reacting $AQ^-(HSI)_2$ trios. Based on our present model, we find that the fast components primarily correspond to the equilibration of the reactant and the intermediate complex.

In the high reactant concentration ($c^{HSI} \to \infty$) and long delay delay ($\tau_{pp} \to \infty$) limit, in Eq. S44 we find that k'_{direct} converges to

$$k_{direct} = k^f_{HSI} \cdot k_{dissoc}/(k^f_{HSI} + k^r_{HSI} + k_{dissoc}) \ll k^f_{HSI} \quad (13)$$

We display relevant trends in Figure 5b. In our previous work,[41] we described the direct reaction of associated pairs as a one-way reaction; the rate of which would then be equal to the thus-defined effective k_{direct}. This description also explains the large covariant error of k^f_{HSI} and k^r_{HSI}: it is k_{direct} that dominates the late-delay response ($\tau_{pp} > 20$ ps), when transient absorption signals are large. The values of $k^{f/r}_{HSI}$ are determined from the early delay region, where the observed signals are relatively small, explaining why we could not accurately determine their values.

We then investigate the activation barrier k_{direct}:

$$E_{direct} = \frac{E^f_{HSI} \cdot (k^r_{HSI} + k_{dissoc})}{k^f_{HSI} + k^r_{HSI} + k_{dissoc}}$$
$$+ \frac{-E^r_{HSI} \cdot k^r_{HSI} + E_{dissoc} \cdot (k^f_{HSI} + k^r_{HSI})}{k^f_{HSI} + k^r_{HSI} + k_{dissoc}} \quad (14)$$

See Eq. S46. To find a more practical form to this, in Eq. S54 we also derive that

$$E_{direct} = \beta^{-1} \cdot (1 - \chi) \cdot \ln[(\chi^{-1} - 1)/(\psi^{-1} + 1)]$$
$$+ E^r_{HSI} \cdot (1 - \chi)/(1 + \psi)$$
$$+ E_{dissoc} \cdot (\chi + \psi)/(1 + \psi) \quad (15)$$

Here we used the substitutions of $\chi = k_{direct}/k_{dissoc}$ and $\psi = k^r_{HSI}/k_{dissoc}$. In this equation, E_{direct}, $E_{dissoc} \approx E^{AQ^-*}_{ani}$, and χ can be experimentally determined. With a sufficient approximation of E^r_{HSI}, we can numerically solve the equation to obtain ψ and thus k^r_{HSI}. Similarly to the case of k_{PU}, we neglect E^r_{HSI} to obtain that $k^r_{HSI} \approx (21 \text{ ps})^{-1}$, $E^f_{HSI} = \Delta G^{\#}_{direct} \approx 4.1$ kJ/mol (via Eq. S51), $k^f_{HSI}/k^r_{HSI} \approx 1/5.3$ and $\lambda_{direct} = 1 - k_{direct}/k^f_{HSI} \approx 0.75$.

We thus find that the obtained $k^f_{HSI}/k^r_{HSI} \approx 1/5$ ratio is 90 times higher than the $k^f_{H_2O}/k^r_{H_2O} \approx 1/480$ ratio obtained for the

proton-uptake reaction from water. This acceleration of the forward reaction follows from the fact that succinimide is a much stronger acid[59] than water (pK^{HSI}_a = 9.56 vs p$K^{H_2O}_a$=14), making the intermediate of the reaction more stable ($\Delta G^{\#}_{direct}$ = 4.1 kJ/mol, $\Delta G^{\#}_{PU}$=15 kJ/mol). Interestingly, the effective reaction rate is not accelerated just as much: we observe that $k_{direct}/k_{PU} = 7.5$; much lower than the 90-fold enhancement of the ratios of the forward and reverse reaction rates. This can be explained from the fact that $\lambda_{direct} \approx 0.75$ of the reaction with HSI causes a much stronger slow-down than $\lambda_{PU} \approx 0.4$ of the reaction with water. This is in turn related to the dissociation rate and mechanism of the intermediates: we estimated that $k_{dissoc} \approx k^{AQ^-*}_{ani}$ = $(57 \text{ ps})^{-1}$, versus the much faster $k_{diff} = (3 \text{ ps})^{-1}$ for OH^- in neat water. In the case of the direct reaction with HSI, the much slower k_{dissoc} leads to $\psi = k_{dissoc}/k^r_{HSI} = 1/2.7$. This means that the intermediate reaction complex $HAQ^*\cdots SI^-$ has a large probability of back-reacting to the initial $AQ^-*\cdots$HSI complex, leading to both the strong slow-down of the overall reaction and the increase of its effective energy barrier to the observed 17 kJ/mol. Overall, this clearly illustrates that the effective reaction rate is determined by both the formation of the intermediate reaction complex and its subsequent dissociation into products.

2.6. Discussion

In this section, we discuss differences in our current measurement results when compared to previously published ones. We start with k_{PU}; see Figure 5b. Based on the displayed linear trend fit, at 22 °C we obtain k^{-1}_{PU} = 3.6 ± 0.8 ns; which is close to the edge of the confidence interval for the previously published value of k^{-1}_{PU} = 2.5 ± 1 ns. This difference can be explained from the inclusion of quenching in the present work. As shown in Figure S26, quenching decreases HAQ* signals, leading to an earlier saturation. This means that if we did not include quenching in the description, the obtained k_{PU} would be faster.

Next, we consider the role of the $HAQ^* \cdots OH^-$ intermediate species in the proton-uptake reaction of photoexcited actino-quinol. In the case of photoacids, similar $RO^-*\cdots H^+$ complexes have long been hypothesized, but their spectral signatures have only recently been observed. Steady-state fluorescence spectroscopy was used to report on $RO^-*\cdots H^+$ for the photoacids QCy7 and QCy9 in ice,[65] and time-resolved fluorescence spectroscopy also showed such signals in case of the photoacid SHONI.[24] Compared to these works, we estimate that in the present study the relative concentration of the intermediate complex is quite low, making it very difficult to observe it spectroscopically. This notion is supported by our fluorescence measurements, where at all temperatures the two emission bands from HAQ* and AQ^-*, with a similar shape but different central frequency, are sufficient to accurately reconstruct the emission spectra obtained by exciting AQ^-; see Figures S6 and S7.

We then discuss the reported $k^f_{H_2O}/k^r_{H_2O}$ values, which were strongly influenced by the value of k_{diff}. In an extreme limit, the hydroxide ion would mainly interact with 'slow' water molecules[66] in the solvation shell of HAQ*; which reorganize with the same rate as the molecule reorients. In this case, $k_{diff} \approx k^{AQ^-*}_{ani} = (57 \text{ ps})^{-1}$ and $E_{diff} \approx E^{AQ^-*}_{ani}$=17 kJ/mol (Figure 5b). Using these, we obtain that $\lambda_{PU} = 0.7$, $E^f_{H_2O} = \Delta G^{\#}_{PU} = 9.3$ kJ/mol, $k^r_{H_2O} = (22 \text{ ps})^{-1}$, and $k^f_{H_2O}/k^r_{H_2O} = 1/45$. As such, even in this limit of extremely slow intermediate complex dissociation, we find that $k^r_{H_2O} \gg k^f_{H_2O}$.

Depending on the charge of the photobase, Coulomb effects may arise in the intermediate species, impacting k_{diff} and thus λ_{PU}. While this does not apply to actinoquinol since HAQ is net neutral, it will certainly impact the dissociation of the intermediate complexes of other, charge neutral photo-bases[34,35,46] — such as 5/6-methoxy-quinoline or 5-amino-quinoline. These photobases have a positive conjugate acid, which would likely lead to a smaller k_{diff} due to the Coulomb attraction of OH^-. Overall, such differences between neutral and charged photobases must be kept in mind when comparing the observed reaction rates (k_{PU}) with the thermodynamic driving forces (pK_b^*).

In Figure 5a, we show fit values for K_{assoc}^{pair}. At 22 °C, we obtain $K_{assoc} = 0.66$ M^{-1}, which is larger than the previous $K_{assoc}^{pair} = 0.5$ M^{-1}. Compared with our previous work, we used an updated method to extract K_{assoc}^{pair}. Because this method uses the full spectral information from the recorded data set, we consider that the current results are both more precise and accurate.

In Figure 5d, we show the calculated values for k_{direct}. At 22 °C, we obtained $(k_{direct})^{-1} = 470 \pm 60$ ps, which is somewhat slower than our previous result: $(k_{direct})^{-1} = 360 \pm 80$ ps. While the definition of k_{direct} is slightly different in the previous study, this is not the main reason for the observed difference. Instead, we consider that k_{direct} is not a direct observable but is derived from the enhancement of the HAQ* signal compared to the signal observed during the reaction in neat water. As such, k_{direct} is affected by both the values of k_{PU} and K_{assoc}^{pair}: a slower k_{PU} yields a larger σ^{HAQ*}, which means that a smaller k_{direct} is required to explain the same amount of signal increase. Similarly, a larger K_{assoc}^{pair} means that the signal results from more associated pairs, which also implies a smaller value for k_{direct}. We included this notion in the calculated error in Figure 5d.

We also discuss k_{neut}, see Figure 5c. In the current work, at 22 °C, we obtain $(k_{neut})^{-1} = 85 \pm 33$ ps·M, instead of our previous result $(k_{neut})^{-1} = 50 \pm 11$ ps·M. We previously assessed that the neutralization pathway dominates at lower c^{HSI}, where the observable SI$^-$ signal strongly affects the determination of k_{neut}. We thus recognize that k_{PU}, and also the normalization of the $c^{HSI} = 0.1$ M signals are both critical in the determination of k_{neut}. We additionally assess that k_{neut} is indirectly dependent on K_{assoc}^{pair}: variations to K_{pair}^{assoc} do not greatly influence the ratio of σ^{HAQ*} and σ^{SI^-}, but alter the relative contribution of the direct reaction pathway at low c^{HSI}. This means that with a larger K_{pair}^{assoc}, a smaller contribution is attributed to the neutralization pathway, yielding a smaller value of k_{neut}. We thus conclude that differences in k_{PU}, the signal normalization approach and in K_{assoc}^{pair} all affect k_{neut}. Ultimately, we consider that it is the presence of multiple competing reaction pathways that makes it difficult to accurately determine k_{neut}. Eliminating the direct reaction pathway, e.g., by using irreversible, Arrhenius-type photobase generators with a quick OH$^-$ release reaction,[67] might yield a more accurate value for k_{neut}.

We then consider possible improvements to our reaction model; see the fit residuals in Figure S30. We find that the residuals primarily appear in a narrow region around 1558 cm^{-1}, attributable to HAQ contributions. To improve these, we need a more accurate quenching model for HAQ*, which, in turn, would yield a more accurate value for both k_{PU} and k_{direct}. To this purpose, we would need a more accurate value for k_{fl}^{HAQ*}, which could be measured via time-resolved single photon counting (TCSPC), and transient absorption measurements with differ-

ent c^{AQ^-}, to allow a more accurate determination of the concentration trends.

We also assess the dynamics of HAQ* and SI$^-$. Currently, we describe reactions occurring in two distinct environments, where AQ^{-}* is hydrogen-bonded to either H$_2$O, or to HSI. In a more statistical description, both environments would have a spectrum of configurations, each with slight variations in the perceived fluctuations[68] and reaction rates. In particular, we consider that the presence of an additional HSI near an AQ^{-}*⋯HSI pair can impact the reaction in two main ways. First, a nearby HSI can impact the solvation dynamics of the intermediate HAQ*⋯SI$^-$ pair. Solvent relaxation effects have been previously described to limit the proton release reaction by reversible photoacids.[17,19] In this work, we find that the solvation of AQ^{-}* can be described with time-constants up to 6 ps; which has a magnitude similar to $(k_{HSI}^r)^{-1} \approx 21$ ps. Because of the proximity of the rate constants, a nearby HSI could alter k_{solv} following a forward proton-uptake reaction ($k_{H_2O}^f$ or k_{HSI}^f) and thereby impact k_{HSI}^r and the net k_{direct}. An alternate way a nearby HSI can accelerate the reaction is by participating in it via an additional reaction step: the extra HSI can react with the hydrogen-bonded SI$^-$ of the HAQ*⋯SI$^-$ pair. This in turn eliminates the chance of a reverse direct reaction, thereby increasing the observed k_{direct}.

Finally, we assess the generality of our results and their applicability to other reaction types. In our work, we described reactions in which reactants require a large degree of orientational correlation. The presented formalism connects the observable reaction rates, their activation barriers, and the underlying forward–reverse reaction rates. We expect that our formalism can be readily applied to other bimolecular reactions where orientational correlation is similarly required, e.g., to enzymatic reactions,[69] or to proton-coupled electron transfer reactions.[70]

3. CONCLUSIONS

We study the mechanism of the light-triggered proton-uptake reaction of the reversible photobase actinoquinol with water using temperature-dependent fluorescence and ultrafast mid-infrared transient absorption experiments. We find that this reaction can be described well with a two-step reaction mechanism. Initially, an intermediate state is formed, consisting of a protonated photobase that remains hydrogen-bonded to the hydroxide ion, that can either dissociate or undergo a reverse reaction. Compared to the initial reaction step, this competition slows the overall reaction down by ~40%, and increases the activation barrier of the net reaction from 15 to 22 kJ/mol.

We additionally study the bimolecular reaction of photo-excited actinoquinol and the weak acid succinimide, which proceeds through two parallel channels. In the first channel, succinimide scavenges a hydroxide generated with the above mechanism; with a rate that is largely constant above 22 °C but lower below. In the second channel, a proton is transferred directly from succinimide to the photoactivated actinoquinol, with a mechanism similar to that with water, i.e., involving an intermediate complex that can either dissociate or back-react to the original complex. Compared to the initial reaction step, the overall reaction is ~70% slower, while the activation barrier is increased from 4 to 17 kJ/mol.

With both water and succinimide as a reaction partner, the reverse reaction is faster than the forward reaction, by 480 and 5 times. This results from the energetically unfavorable formation

of the intermediate complex, the energy penalty of which is higher with water than that with the more acidic succinimide. We anticipate that the presented reaction model can be applied to other reaction types where the reactants' orientational correlation is similarly critical, such as enzymatic or proton-coupled electron transfer reactions.

4. EXPERIMENTAL METHODS

Below we provide a short summary of our approach to experimental methods and chemical samples. Most of our experimental methods follow those defined in our previous work.[41] In certain cases, an additional description is available in the Supporting Information.

4.1. Chemicals

We used a Simplicity Millipore system to obtain purified H_2O with a resistivity of 18.2 MΩ ·cm. Additional chemicals were used as received from TCI Chemicals Europe, Merck/Sigma-Aldrich, and Fluka/Honeywell; see Table S1. When not in use, we stored these chemicals in closed containers under nitrogen atmosphere in the dark.

4.2. Sample Preparation Methods

To prepare samples, we dissolved/diluted pure chemicals to create stock solutions with high concentrations. We then created target solutions by mixing these stock solutions in a predetermined amount. To ensure that the listed dyes are not subject to UV light before using them, we prepared samples containing these under special lighting conditions without blue or UV light present. Last, to ensure that the pH of solutions with actinoquinol is in the 6−8 range, we added a small, calculate amount of NaOH to each; thus preventing buffering effects from HSI and ambient CO_2 content.

4.3. Density Measurement and Concentration Calculation

To accurately determine the concentration of individual samples at different temperatures, we first calculated the mass ratio x_m^{solute} of a solute. Using this, we can calculate the absolute concentration of chemicals in each sample at each temperature:

$$c^{solute} = x_m^{solute} \cdot \frac{\rho^{solution}(x_m,\ T)}{M^{solute}} \tag{16}$$

where M^{solute} denotes the molar mass of a given solute and $\rho^{solution}$ denotes the density of the entire solution.

In particular, for samples containing both 5−20 mM AQ⁻ and varying concentration of HSI, we approximated that the presence of AQ⁻ does not change the density of the solution.

To determine $\rho^{solution}(x_m,\ T)$, we used a Mettler-Toledo DM40 density meter; which is much more accurate than the previous approach using a pipet and an analytical scale. We calibrated this density meter with the density of air and ultrapure water at T = 22 °C. For solutions containing a varying amount of HSI, we then measured individual data points at different temperatures, see Figure S2. We then used a second-order polynomial to fit each data point, see Eq. S1. We then used the density curve ρ^{fit} to calculate the concentrations of solutions of interest.

4.4. Steady-State Fluorescence Experiments

To perform simultaneously recorded absorption and fluorescence emission measurements (SAFE[71−73]), we used a HORIBA Duetta-Bio. Within the device, we collect absorption spectra in a transmission geometry and fluorescence spectra in a right-angle geometry. Emission spectra are factory calibrated and used as-is. Typical settings include data acquisition in the 300−800 nm region, with an excitation/emission slit width of 5 nm; and with magic-angle polarization setting. We additionally enabled the solvent background subtraction and the inner-filtering[74] corrections in the supplied EzSpec software.

When collecting fluorescence spectra, we used dye solutions with a few μM concentration. As a rule of thumb, we adjusted the solution concentration until the total decadic absorbance (A) was less than 0.15. We put liquid samples in Thorlabs CV10Q35FAE chemically resistant fused silica cuvettes, placed in the temperature-controlled SampleS-nap4-Pelt sample holder set. For quantum yield calibration, reference dye spectra were recorded at T = 22 °C. In general, we stirred all

samples with a small, magnetic stirring bead at 2000 rpm. After measurements, we used the recommended 'drop and drag' cleaning methods by Thorlabs[75] for the exterior of the cuvettes. To rinse the cuvette interior, we used a cuvette fountain with water and then ethanol and then dried the cuvette insides with nitrogen flush.

Because of the calibration performed by Horiba, the recorded spectra are defined as it follows: $I_\lambda^{rel} \propto t_{int}^{-1} \cdot \frac{\partial E}{\partial \lambda}$ with E = sampled energy, t_{int} = integration time. We convert these spectra to photon emission density spectra: $\rho_\varepsilon^{rel} = \frac{I_\lambda^{rel}}{\varepsilon^3} \cdot n(\varepsilon)^2$. The n^2 refractive index term here corrects for wavelength-dependent solid angle changes.

As the next step in data processing, we used our previously established excitation correction algorithm. Following a service visit, we chose to recalibrate our device. In this process, we integrate emitted photon density spectra (ρ_ε^{rel}) over the entire emission wavelength range, to obtain device-specific fluorescence quantum yields (Φ_f^{device}) at different excitation wavelengths: $\Phi_f^{device} = \int \rho_\varepsilon(\varepsilon_{exc}, \varepsilon_{em})\ d\varepsilon_{em} \cdot A^{-1}(\varepsilon_{exc})$. Using this method, we overlap the obtained curves, yielding a relative excitation factor; see Figure S3.

With this, we can calibrate our device to yield a value of Φ_f. Here, we follow our previous procedure and reference the device-specific quantum yields with literature-reported quantum yields; see Figure S4.

4.5. Steady-State UV Absorption Experiments

To obtain quantitative UV−vis spectra at different temperatures, we used Horiba Duetta-Bio. We placed liquid samples in 2 Thorlabs CV10Q7FA cuvettes placed, which have a beam-path of 2 mm. From each measurements, we subtracted the signals of a H_2O-filled cuvette, which account for cuvette reflections. We then matched the path lengths of the two cuvettes, by measuring the absorption of an identical 0.4 mM HAQ solution. We found that the path lengths differ by >2%. We then used this factor to compensate for the path length differences and took the average length of the two cuvettes to be the specified 2 mm. We then recorded absorption spectra with 3 nm step size and slit width in the 275−600 nm spectral region. For each temperature setting, we first waited for the SampleSnap4 sample holder to thermalize (read out with an internal temperature sensor), then waited an additional 7 min to ensure that the cuvettes and their contents are thermalized to a great accuracy. To avoid cuvette fogging in the case of measurements at lower than ambient temperatures, we gently flushed the sample compartment with N_2; which helps by lowering the dew point.

By recreating measurement conditions identical to our previous work, we obtained the "empty triangle" measurement point in Figure 5a. Here, we used a PerkinElmer Lambda 35 spectrometer, with a 1 nm slit width and step size in the 275−600 nm spectral region. We injected liquid samples with ≈10 mM AQ⁻ concentration in a Starna Ultra-Micro 100 μm fixed thickness UV silica flowcell. For cleaning, we recreated the processes used for the fluorescence cuvettes. We determine the cuvette thickness by analyzing the fringe spacing in the transmission spectrum of the empty cell. We then used this to calculate decadic molar attenuation coefficients ϵ_{att} for each sample, after subtracting the UV−vis spectrum of a H_2O-filled cuvette. To determine the thickness of this cuvette, we analyzed the fringes that appear in its transmission spectrum when the cuvette is filled with air. We last measured the temperature of the lab as the temperature of the liquid measured, which was T = 21 °C.

4.6. Steady-State Infrared Absorption Experiments

We recorded infrared absorption spectra with a Bruker Vertex 80v Fourier transform spectrometer with a resolution of 1 cm⁻¹. Liquid samples were sandwiched between 0.5 mm thick UV grade CaF_2 windows (Crystran CAFP25.4-0.5U), separated by 25 μm thick, chemically inert fluorinated ethylene propylene (FEP) spacers. After each measurement, we cleaned windows using the 'drop and drag' method, using water and then ethanol. During measurements, we purged the sample compartment with N_2 to prevent ambient absorption of CO_2 and H_2O vapor.

To subtract solvent absorption features, we followed our previous routine.[41] First, to suppress interference fringes due to the similar thickness of the two windows, we use Fourier-filtering at carefully

selected frequencies that do not meaningfully impact the observed spectral features. We then identify spectral region specific to solvent features (e.g., H_2O, hydrated H^+, hydrated OH^-). We then perform a serial subtraction of CaF_2 (double thickness, reflection corrected) and other solvent features (H_2O, then added H^+/OH^-) to retrieve the solute spectra. Compared to our previous work, our device has aged and now has few mOD baseline fluctuations between measurements. To account for these, in the subtraction step of H_2O we additionally identify the small offset, that yields the closest-to-zero baseline in the spectral region selected for H_2O. Last, we additionally scale each spectrum with the solute concentration and the relative amount of the subtracted H_2O spectra, to obtain quantitatively comparable absorption spectra.

4.7. Transient Absorption Experiments

In our home-built experimental setup, we generate near-infrared (NIR) laser pulses using a Light-Conversion Pharos PH1 amplifier system (1 kHz, 1026 nm, 400 μJ, 300 fs). We then split and delay a small portion of these with the help of two delay stages (Newport and Physik Instrumente). The two delay stages together allow for a delay of 2.3 ns. To align the 1026 nm beam parallel to the motion of the delay stages, we developed a small application based on a CMOS camera (Basler Dart daA1920−160um). Within an alignment iteration, the camera, mounted on the stage, records the beam profile at different stage positions, which we use to calculate the misalignment. After each scan, the program displays the current misalignment and prompts the user to adjust it. The user stops the alignment process when the beam misalignment is smaller than 35 μrad, calculated as the average for three successive scans with no alignment between. We focus the thus delayed NIR pulses onto a doubling and a tripling BBO crystal; yielding 342 nm (29240 cm^{-1}, 3.63 eV) UV pulses. After recollimation, we used ND filters to decrease the UV pulse energy to a typical value of 1.3 μJ. Using a $\lambda/2$ waveplate, we then adjusted the beam polarization.

We generated MIR pulses around 6.66 μm (0.186 eV, 1500 cm^{-1}), using a Light-Conversion Orpheus One HP optical parametric amplifier with a built-in difference-frequency-generation step. These pulses have a typical 3.5 μJ energy right after the amplifier. In the experimental setup, the MIR pulses are split to probe and reference paths, which are separately attenuated using a pair of wire-grid polarizers. To ensure low absorption by ambient H_2O vapor in the air, we purified the atmosphere in our experimental setup with dry air.

Using a lens and a parabolic mirror, we focus the UV and MIR pulses onto the liquid sample in a sample cell. We focused the pump and probe pulses onto the same spot and referenced pulses onto another spot. To always illuminate a fresh spot of the sample, we rotated the sample cell at 1000 rpm. To ensure accurate thermal contact, we used exterior copper spacers between the sample cell and the enclosing holder. After the sample cell, the pump beam is blocked and the MIR beams pass through a computer-controlled polarizer, adjusted in pump-parallel and pump-perpendicular settings. We then recollimate and refocus these beams onto the input slit of our spectrometer. In the sample plane, both beams are focused onto separate MCT detector arrays (Infrared Associates). Compared to our previous work, we use a newer detector and thus have an improved signal-to-noise ratio. We then use the thus recorded polarization-resolved transient absorption data to construct isotropic spectra: $\Delta A_{iso} = \frac{\Delta A_{\parallel} + 2\cdot\Delta A_{\perp}}{3}$.

The sample cell is additionally heated/cooled with a temperature controlled chiller. After thermalization, we read the sample temperature as the body temperature of the sample rotator and round it to an integer value before displaying in the main text. To ensure no heat transfer between the sample rotator and the optical table, we used a heat-insulating plastic mounting plate between the rotator and the mount holder.

To obtain the best ΔA_{iso} spectra, we performed a two-axis knife edge analysis in the approximate sample plane. We selected the sample plane position and the UV lens focusing position to yield spots with approx 130×110 μm fwhm size, and MIR pulses with approximately 70×100 μm fwhm size. Because of our long maximal delay achieved with the two delay stages, we additionally performed knife-edge analysis of the UV

pump spot at various τ_{pp} delay points. Here, we find that the width and the power of the UV pulse changes approximately linearly with the delay, with 4% and <1%, respectively. By evaluating the pump−probe integral over the sample surface S at each delay point:

$$\Delta A_{iso} \propto \frac{\int_S I_{probe}\cdot I_{pump}\cdot dS}{\int_S I_{probe}\cdot dS} \tag{17}$$

we obtain instrument-specific sensitivity factors, on the scale of a few %. We then use the inverse of these to correct for our experimental data. We additionally find that in the approximate sample plane, the probe beam's walk-off is within ±2 μm.

To identify the temporal overlap of the probe and reference pulses, we monitor the nonresonant ΔA_{iso} signals, recorded in solvent-filled cells.[76] By analyzing such signals, we set the zero-delay point with <50 fs accuracy and find the instrument response to be ~400 fs long.

ASSOCIATED CONTENT

Supporting Information

The Supporting Information is available free of charge at https://pubs.acs.org/doi/10.1021/jacsau.4c00326.

Description of additional experimental details and data processing approaches; as well as supporting spectroscopic measurements. This file additionally contains charts with all plotted (error) values in Figures 1c, 2, and 5 (PDF)

AUTHOR INFORMATION

Corresponding Authors

Balázs Antalicz − *AMOLF, Ultrafast Spectroscopy, 1098 XG Amsterdam, The Netherlands;* orcid.org/0000-0002-7918-8688; Email: antalicz@amolf.nl

Huib J. Bakker − *AMOLF, Ultrafast Spectroscopy, 1098 XG Amsterdam, The Netherlands;* orcid.org/0000-0003-1564-5314; Email: bakker@amolf.nl

Complete contact information is available at:
https://pubs.acs.org/10.1021/jacsau.4c00326

Author Contributions

B.A. and H.J.B. designed the research. B.A. performed the experiments, analyzed the data, and performed the theoretical derivations. All authors discussed the results. B.A. wrote the initial manuscript, and all authors finalized the manuscript together. CRediT: **Balázs Antalicz** conceptualization, data curation, formal analysis, investigation, methodology, project administration, resources, software, validation, visualization, writing-original draft, writing-review & editing; **Huib J. Bakker** conceptualization, funding acquisition, project administration, resources, supervision, validation, writing-review & editing.

Notes

The authors declare no competing financial interest.

additionally thank Cristoph Kaiser, Alexander Korotkevich, and Jan Versluis for fruitful discussions about physical chemistry.

■ REFERENCES

(1) Mikulski, R. L.; Silverman, D. N. Proton transfer in catalysis and the role of proton shuttles in carbonic anhydrase. *Biochimica et Biophysica Acta (BBA)-Proteins and Proteomics* **2010**, *1804*, 422−426.

(2) Kramer, D. M.; Avenson, T. J.; Edwards, G. E. Dynamic flexibility in the light reactions of photosynthesis governed by both electron and proton transfer reactions. *Trends in plant science* **2004**, *9*, 349−357.

(3) Pielak, R. M.; Chou, J. J. Influenza M2 proton channels. *Biochimica et Biophysica Acta (BBA)-Biomembranes* **2011**, *1808*, 522−529.

(4) Ivanovic, T.; Rozendaal, R.; Floyd, D. L.; Popovic, M.; Van Oijen, A. M.; Harrison, S. C. Kinetics of proton transport into influenza virions by the viral M2 channel. *PloS one* **2012**, *7*, e31566.

(5) Liu, L.; Bakker, H. J. Vibrational excitation induced proton transfer in hydrated Nafion membranes. *J. Phys. Chem. B* **2015**, *119*, 2628−2637.

(6) Phun, G. S.; Bhide, R.; Ardo, S. Detailed-balance limits for sunlight-to-protonic energy conversion from aqueous photoacids and photobases based on reversible mass-action kinetics. *Energy Environ. Sci.* **2023**, *16*, 4593−4611.

(7) Nocera, D. G. Proton-coupled electron transfer: the engine of energy conversion and storage. *J. Am. Chem. Soc.* **2022**, *144*, 1069−1081.

(8) Demchenko, A. P. Proton transfer reactions: from photochemistry to biochemistry and bioenergetics. *BBA Advances* **2023**, *3*, 100085.

(9) White, W.; Sanborn, C. D.; Fabian, D. M.; Ardo, S. Conversion of visible light into ionic power using photoacid-dye-sensitized bipolar ion-exchange membranes. *Joule* **2018**, *2*, 94−109.

(10) Nocera, D. G. The artificial leaf. *Accounts of chemical research* **2012**, *45*, 767−776.

(11) Haghighat, S.; Ostresh, S.; Dawlaty, J. M. Controlling proton conductivity with light: a scheme based on photoacid doping of materials. *J. Phys. Chem. B* **2016**, *120*, 1002−1007.

(12) Halbritter, T.; Kaiser, C.; Wachtveitl, J.; Heckel, A. Pyridine-spiropyran derivative as a persistent, reversible photoacid in water. *Journal of organic chemistry* **2017**, *82*, 8040−8047.

(13) Yucknovsky, A.; Amdursky, N. Controlling pH-Sensitive Chemical Reactions Pathways with Light-a Tale of Two Photobases: an Arrhenius and a Brønsted. *Chem.—Eur. J.* **2023**, *30*, e202303767.

(14) Wimberger, L.; Prasad, S. K.; Peeks, M. D.; Andréasson, J.; Schmidt, T. W.; Beves, J. E. Large, tunable, and reversible pH changes by merocyanine photoacids. *J. Am. Chem. Soc.* **2021**, *143*, 20758−20768.

(15) Fu, C.; Xu, J.; Boyer, C. Photoacid-mediated ring opening polymerization driven by visible light. *Chem. Commun.* **2016**, *52*, 7126−7129.

(16) Yeo, H.; Khan, A. Photoinduced proton-transfer polymerization: A practical synthetic tool for soft lithography applications. *J. Am. Chem. Soc.* **2020**, *142*, 3479−3488.

(17) Leiderman, P.; Gepshtein, R.; Uritski, A.; Genosar, L.; Huppert, D. Temperature dependence of excited-state proton transfer in water electrolyte solutions and water- methanol solutions. *J. Phys. Chem. A* **2006**, *110*, 9039−9050.

(18) Cohen, B.; Huppert, D. Unusual temperature dependence of excited state proton transfer rates in alcohols. *J. Phys. Chem. A* **2000**, *104*, 2663−2667.

(19) Cohen, B.; Leiderman, P.; Huppert, D. Unusual temperature dependence of proton transfer. 2. Excited-state proton transfer from photoacids to water. *J. Phys. Chem. A* **2002**, *106*, 11115−11122.

(20) Cohen, B.; Segal, J.; Huppert, D. Proton transfer from photoacid to solvent. *J. Phys. Chem. A* **2002**, *106*, 7462−7467.

(21) Tolbert, L. M.; Solntsev, K. M. Excited-state proton transfer: from constrained systems to super photoacids to superfast proton transfer. *Acc. Chem. Res.* **2002**, *35*, 19−27.

(22) Kaiser, C.; Halbritter, T.; Heckel, A.; Wachtveitl, J. Proton-Transfer Dynamics of Photoacidic Merocyanines in Aqueous Solution. *Chem.—Eur. J.* **2021**, *27*, 9160−9173.

(23) Kumpulainen, T.; Bakker, B. H.; Hilbers, M.; Brouwer, A. M. Synthesis and spectroscopic characterization of 1, 8-naphthalimide derived super photoacids. *J. Phys. Chem. B* **2015**, *119*, 2515−2524.

(24) Verma, P.; Rosspeintner, A.; Dereka, B.; Vauthey, E.; Kumpulainen, T. Broadband fluorescence reveals mechanistic differences in excited-state proton transfer to protic and aprotic solvents. *Chemical Science* **2020**, *11*, 7963−7971.

(25) Rini, M.; Magnes, B.-Z.; Pines, E.; Nibbering, E. T. Real-time observation of bimodal proton transfer in acid-base pairs in water. *Science* **2003**, *301*, 349−352.

(26) Rini, M.; Pines, D.; Magnes, B.-Z.; Pines, E.; Nibbering, E. T. Bimodal proton transfer in acid-base reactions in water. *J. Chem. Phys.* **2004**, *121*, 9593−9610.

(27) Cox, M. J.; Timmer, R. L.; Bakker, H. J.; Park, S.; Agmon, N. Distance-dependent proton transfer along water wires connecting acid-base pairs. *J. Phys. Chem. A* **2009**, *113*, 6599−6606.

(28) Chiariello, M. G.; Raucci, U.; Donati, G.; Rega, N. Water-mediated excited state proton transfer of pyranine-acetate in aqueous solution: Vibrational fingerprints from ab initio molecular dynamics. *J. Phys. Chem. A* **2021**, *125*, 3569−3578.

(29) Siwick, B. J.; Bakker, H. J. On the role of water in intermolecular proton-transfer reactions. *J. Am. Chem. Soc.* **2007**, *129*, 13412−13420.

(30) Shin, J.; Lim, C. H.; Lim, M. Photoacid-induced aqueous acid-base reactions probed by femtosecond infrared spectroscopy. *Photochemical & Photobiological Sciences* **2022**, *21*, 1419−1431.

(31) Cohen, B.; Huppert, D.; Agmon, N. Non-Exponential Smoluchowski Dynamics in Fast Acid- Base Reaction. *J. Am. Chem. Soc.* **2000**, *122*, 9838−9839.

(32) Cox, M.; Bakker, H. Femtosecond study of the deuteron-transfer dynamics of naphtol salts in water. *J. Phys. Chem. A* **2010**, *114*, 10523−10530.

(33) Joung, J. F.; Lee, J.; Hwang, J.; Choi, K.; Park, S. A new visible light triggered Arrhenius photobase and its photo-induced reactions. *New J. Chem.* **2020**, *44*, 668−673.

(34) Driscoll, E. W.; Hunt, J. R.; Dawlaty, J. M. Proton capture dynamics in quinoline photobases: substituent effect and involvement of triplet states. *J. Phys. Chem. A* **2017**, *121*, 7099−7107.

(35) Hunt, J. R.; Dawlaty, J. M. Photodriven deprotonation of alcohols by a quinoline photobase. *J. Phys. Chem. A* **2018**, *122*, 7931−7940.

(36) Sheng, W.; Nairat, M.; Pawlaczyk, P. D.; Mroczka, E.; Farris, B.; Pines, E.; Geiger, J. H.; Borhan, B.; Dantus, M. Ultrafast dynamics of a "Super" photobase. *Angew. Chem., Int. Ed.* **2018**, *57*, 14742−14746.

(37) Lahiri, J.; Moemeni, M.; Kline, J.; Borhan, B.; Magoulas, I.; Yuwono, S. H.; Piecuch, P.; Jackson, J. E.; Dantus, M.; Blanchard, G. Proton Abstraction Mediates Interactions between the Super Photobase FR0-SB and Surrounding Alcohol Solvent. *J. Phys. Chem. B* **2019**, *123*, 8448−8456.

(38) Pines, E.; Huppert, D.; Gutman, M.; Nachliel, N.; Fishman, M. The pOH jump: determination of deprotonation rates of water by 6-methoxyquinoline and acridine. *J. Phys. Chem.* **1986**, *90*, 6366−6370.

(39) Naik, L.; Suresh Kumar, H.; Inamdar, S.; Math, N. Steady-State and Time-Resolved Emission Studies of 6-Methoxy Quinoline. *Spectroscopy letters* **2005**, *38*, 645−659.

(40) Sittig, M.; Tom, J. C.; Elter, J. K.; Schacher, F. H.; Dietzek, B. Quinoline Photobasicity: Investigation within Water-Soluble Light-Responsive Copolymers. *Chem.—Eur. J.* **2021**, *27*, 1072−1079.

(41) Antalicz, B.; Versluis, J.; Bakker, H. J. Observing Aqueous Proton-Uptake Reactions Triggered by Light. *J. Am. Chem. Soc.* **2023**, *145*, 6682−6690.

(42) Tuckerman, M. E.; Chandra, A.; Marx, D. A statistical mechanical theory of proton transport kinetics in hydrogen-bonded networks based on population correlation functions with applications to acids and bases. *J. Chem. Phys.* **2010**, *133*, 124108.

(43) Marx, D.; Chandra, A.; Tuckerman, M. E. Aqueous basic solutions: hydroxide solvation, structural diffusion, and comparison to the hydrated proton. *Chem. Rev.* **2010**, *110*, 2174−2216.

(44) Chen, M.; Zheng, L.; Santra, B.; Ko, H.-Y.; DiStasio, R. A., Jr; Klein, M. L.; Car, R.; Wu, X. Hydroxide diffuses slower than hydronium

in water because its solvated structure inhibits correlated proton transfer. *Nature Chem.* **2018**, *10*, 413−419.

(45) Driscoll, E. W.; Hunt, J. R.; Dawlaty, J. M. Photobasicity in Quinolines: Origin and Tunability via the Substituents' Hammett Parameters. *J. Phys. Chem. Lett.* **2016**, *7*, 2093−2099.

(46) Alamudun, S. F.; Tanovitz, K.; Fajardo, A.; Johnson, K.; Pham, A.; Jamshidi Araghi, T.; Petit, A. S. Structure-Photochemical Function Relationships in Nitrogen-Containing Heterocyclic Aromatic Photobases Derived from Quinoline. *J. Phys. Chem. A* **2020**, *124*, 2537−2546.

(47) Siano, D. B.; Metzler, D. E. Band shapes of the electronic spectra of complex molecules. *J. Chem. Phys.* **1969**, *51*, 1856−1861.

(48) Burstein, E. A.; Emelyanenko, V. I. Log-normal description of fluorescence spectra of organic fluorophores. *Photochem. Photobiol.* **1996**, *64*, 316−320.

(49) Gould, I. R.; Boiani, J. A.; Gaillard, E. B.; Goodman, J. L.; Farid, S. Intersystem crossing in charge-transfer excited states. *J. Phys. Chem. A* **2003**, *107*, 3515−3524.

(50) Berg, H. C. *Random walks in biology*; Princeton University Press, 1993.

(51) Nakahara, M.; Wakai, C. *Studies in Physical and Theoretical Chemistry*; Elsevier, 1995; Vol. *83*; pp 149−155.

(52) Nakahara, M.; Wakai, C.; Yoshimoto, Y.; Matubayasi, N. Dynamics of hydrophobic hydration of benzene. *J. Phys. Chem.* **1996**, *100*, 1345−1349.

(53) Petersen, C.; Tielrooij, K.-J.; Bakker, H. J. Strong temperature dependence of water reorientation in hydrophobic hydration shells. *J. Chem. Phys.* **2009**, *130*, 214511.

(54) Nicodemus, R. A.; Corcelli, S.; Skinner, J.; Tokmakoff, A. Collective hydrogen bond reorganization in water studied with temperature-dependent ultrafast infrared spectroscopy. *J. Phys. Chem. B* **2011**, *115*, 5604−5616.

(55) Qvist, J.; Mattea, C.; Sunde, E. P.; Halle, B. Rotational dynamics in supercooled water from nuclear spin relaxation and molecular simulations. *J. Chem. Phys.* **2012**, *136*, 204505.

(56) van der Post, S. T.; Bakker, H. J. Femtosecond mid-infrared study of the reorientation of weakly hydrogen-bonded water molecules. *J. Phys. Chem. B* **2014**, *118*, 8179−8189.

(57) Piskulich, Z. A.; Thompson, W. H. The activation energy for water reorientation differs between IR pump-probe and NMR measurements. *J. Chem. Phys.* **2018**, *149*, 164504.

(58) Piskulich, Z. A.; Laage, D.; Thompson, W. H. On the role of hydrogen-bond exchanges in the spectral diffusion of water. *J. Chem. Phys.* **2021**, *154*, 064501.

(59) Simms, H. S. The effect of salts on weak electrolytes. I. Dissociation of weak electrolytes in the presence of salts. *J. Phys. Chem.* **1928**, *32*, 1121−1141.

(60) Stamboliyska, B.; Binev, Y. I.; Radomirska, V.; Tsenov, J.; Juchnovski, I. IR spectra and structure of 2, 5-pyrrolidinedione (succinimide) and of its nitranion: experimental and ab initio MO studies. *J. Mol. Struct.* **2000**, *516*, 237−245.

(61) Horrocks, D. L. Fluorescence Self-Quenching through Hydrogen Bonding. *J. Chem. Phys.* **1969**, *50*, 4151−4156.

(62) Meskine, H.; Matera, S.; Scheffler, M.; Reuter, K.; Metiu, H. Examination of the concept of degree of rate control by first-principles kinetic Monte Carlo simulations. *Surf. Sci.* **2009**, *603*, 1724−1730.

(63) Mao, Z.; Campbell, C. T. Apparent activation energies in complex reaction mechanisms: a simple relationship via degrees of rate control. *ACS Catal.* **2019**, *9*, 9465−9473.

(64) Roberts, S. T.; Ramasesha, K.; Petersen, P. B.; Mandal, A.; Tokmakoff, A. Proton transfer in concentrated aqueous hydroxide visualized using ultrafast infrared spectroscopy. *J. Phys. Chem. A* **2011**, *115*, 3957−3972.

(65) Simkovitch, R.; Akulov, K.; Shomer, S.; Roth, M. E.; Shabat, D.; Schwartz, T.; Huppert, D. Comprehensive Study of Ultrafast Excited-State Proton Transfer in Water and D2O Providing the Missing RO—···H+ Ion-Pair Fingerprint. *J. Phys. Chem. A* **2014**, *118*, 4425−4443.

(66) van der Post, S. T.; Scheidelaar, S.; Bakker, H. J. Water dynamics in aqueous solutions of tetra-n-alkylammonium salts: Hydrophobic and coulomb interactions disentangled. *J. Phys. Chem. B* **2013**, *117*, 15101−15110.

(67) Xie, Y.; Ilic, S.; Skaro, S.; Maslak, V.; Glusac, K. D. Excited-State Hydroxide Ion Release From a Series of Acridinol Photobases. *J. Phys. Chem. A* **2017**, *121*, 448−457.

(68) Piskulich, Z. A.; Mesele, O. O.; Thompson, W. H. Activation energies and beyond. *J. Phys. Chem. A* **2019**, *123*, 7185−7194.

(69) Cornish-Bowden, A. One hundred years of Michaelis-Menten kinetics. *Perspectives in Science* **2015**, *4*, 3−9.

(70) Weinberg, D. R.; Gagliardi, C. J.; Hull, J. F.; Murphy, C. F.; Kent, C. A.; Westlake, B. C.; Paul, A.; Ess, D. H.; McCafferty, D. G.; Meyer, T. J. Proton-coupled electron transfer. *Chem. Rev.* **2012**, *112*, 4016−4093.

(71) Nawara, K.; Waluk, J. Goodbye to Quinine in Sulfuric Acid Solutions as a Fluorescence Quantum Yield Standard. *Anal. Chem.* **2019**, *91*, 5389−5394.

(72) Nawara, K.; Waluk, J. Fluorescence quantum yield determination using simultaneous double-beam absorption measurement. *Measurement* **2020**, *165*, 108159.

(73) Würth, C.; Grabolle, M.; Pauli, J.; Spieles, M.; Resch-Genger, U. Comparison of methods and achievable uncertainties for the relative and absolute measurement of photoluminescence quantum yields. *Analytical chemistry* **2011**, *83*, 3431−3439.

(74) MacDonald, B. C.; Lvin, S. J.; Patterson, H. Correction of fluorescence inner filter effects and the partitioning of pyrene to dissolved organic carbon. *Analytica chimica acta* **1997**, *338*, 155−162.

(75) Optics Handling and Care Tutorial. *ThorLabs.* https://www.thorlabs.com/newgrouppage9.cfm?objectgroup_id=9025.

(76) Agrawal, G. P.; Baldeck, P.; Alfano, R. Temporal and spectral effects of cross-phase modulation on copropagating ultrashort pulses in optical fibers. *Phys. Rev. A* **1989**, *40*, 5063.